Received: 06 March 2026 | **Revised:** 01 April 2026 | **Accepted:** 07 April 2026 Science Research Annals—Physical Sciences 2(1), 1–12

SCIENCE RESEARCH ANNALS
(PHYSICAL SCIENCES)

Published by the Faculty of Science, Adekunle Ajasin University, Akungba-Akoko (AAUA)

Journal website: https://sra.com.ng/index.php/sra-physical

SCIENTIFIC ARTICLE DOI: https://doi.org/10.63112/ne611a08

Magnetohydrodynamic free convection nanofluid flow over a convectively heated vertical disk with non-uniform heat generation and nonlinear radiation

Ephesus O. Fatunmbi [1, *]

[1] *Department of Mathematics and Statistics, Federal Polytechnic Ilaro, PMB 50, Ilaro, Ogun State, Nigeria*

*Correspondence: ephesus.fatunmbi@federalpolyilaro.edu.ng (E.O. Fatunmbi)

ARTICLE INFORMATION

Keywords:
Free convective flow
Magneto-nanofluid
Convective heating
Nonuniform heating
Nonlinear thermal radiation

Handling Editor: A. S. Oke

ABSTRACT

Magnetohydrodynamic (MHD) nanofluid flows have become very popular in modern alternative thermal systems, such as solar collector systems, electronic cooling devices, and high-temperature industrial processes involving high-performance heat regulation processes. In connection with these applications in various thermal systems, the current study investigates free convective MHD nanofluid flow over a vertical disk under the influence of convective heating, non-uniform heating source, and nonlinear thermal radiation. By using similarity transformations to remodel the governing equations from partial differential equations into coupled nonlinear ordinary differential equations, the complete set of these equations is numerically integrated by combining the shooting technique with a fourth-order Runge-Kutta algorithm. The impact of key physical parameters on various dimensionless profiles is analyzed through various graphs. The results of the analysis indicate that the magnetic field term decelerates velocity due to the presence of Lorentz forces, both spatial and thermal-dependent heat sources thicken the thermal bounding layer and affect heat transfer distribution in the system. More so, convective heating and nonlinear thermal radiation produce higher temperatures in the system. These results provide valuable insight into the potential improvements in terms of efficiency and control of MHD-based energy systems and industrial heat transfer applications.

Highlights

- Thermophoresis raises temperature and nanoparticle concentration profiles.
- Brownian motion reduces concentration distribution in the boundary layer.
- Magnetic, porosity and Forchheimer terms suppress fluid velocity.
- Heat source terms increase temperature and thicken thermal boundary layer.
- Activation energy boosts concentration; reaction shrinks solutal layer.

1. Introduction

Free convection is an essential part of modern thermo-fluid systems that improves thermal performance, controls boundary-layer behaviour, and reduces energy loss in many systems. This phenomenon results from variation in buoyancy forces caused by temperature or concentration gradients in a fluid. This induces a change in density and is very important in many engineering fields, such as solar thermal systems, nuclear energy systems, electronic cooling systems, and chemical processing equipment (Umavathi et al., 2016; Kumar, 2001; Abro, 2020; Jha et al., 2022). Researchers have conducted studies to investigate free convection flow behaviour through various fluid dynamics and physical characteristics. For instance, the study conducted by Seth et al. (2019) showed that partial slip conditions significantly affected heat and momentum transfer during viscoelastic free convection flow through nonlinearly stretching surfaces. Chamkha et al. (2019) studied the impacts of viscous dissipation on free convection of Cu-water nanofluid through a porous enclosure that contained internal heat generation, demonstrating improved thermal conductivity. Abro et al. (2020) used fractional and statistical techniques to investigate the properties of magnetized free convection flow together with its thermal resistance behaviour, while Fatunmbi et al. (2022) studied buoyancy and slip impact

on hydromagnetic micropolar fluid flow passing an exponentially stretching sheet. Ahmed et al. (2023) expanded analogous research to a vertically stretching disk, incorporating Brownian motion and thermophoresis. Even with these contributions, making real-world systems more thermally efficient needs advanced heat transfer fluids that can move energy better, like nanofluids.

Nanofluids are a colloidal mixture of base fluids like oil, water, etc., with minute nanoparticles (Choi, 1995). This advanced fluid, through MHD actions, found crucial application in heat transfer systems, such as in solar collectors and electronic cooling systems. MHD nanofluids also operate at high temperatures in many industrial applications where precise temperature control of the heat transfer fluid is required (Dinarvand & Pop, 2027). The dispersion of nanoparticles significantly improves the thermophysical properties of base fluids, enabling diverse applications in transport and automotive engineering, pharmaceutical and drug manufacturing, solar energy systems, heat exchangers, electronic device cooling, aerospace thermal management, and biomedical drug delivery (Alao et al., 2020; Devendiran, 2016; Nadeem, 2016; Mishra,2021). Several nanofluid models have been proposed in the literature; however, the Buongiorno model distinctly identifies Brownian motion and thermophoresis as the dominant mechanisms responsible for nanoparticle transport (Fatunmbi et al., 2020; Nadeem, 2016; Mishra2021; Turkyilmazoglu, 2017 & 2021; Fatunmbi et al., 2023). This model introduces additional terms into the energy and nanoparticle concentration equations, providing a more realistic description of coupled heat-mass transfer processes.

Among the important heat transfer mechanisms in engineering applications, non-uniform heat sources and convective heating play significant roles. The former is characterized by spatially varying heat supply, chemical reactions, and internal heat generation, while the latter describes the heat transfer process from a solid surface to the adjacent fluid, typically using convective boundary conditions and heat transfer coefficients along with ambient fluid temperatures. These two heat transfer processes find applications in many areas, such as non-uniform heat sources in solar energy, micro-electronics, chemical reactors, and nuclear reactors, while convective heating is commonly found in heat exchangers, electronic components, polymer processing, and aerospace applications.

Previous research has demonstrated that non-uniform heat sources create major changes in both fluid movement and heat transfer processes. Muthtamilselvan et al. (2017) studied natural convection in a micropolar fluid with both constant and variable heat production, which resulted in major shifts in both thermal and velocity patterns. Thumma et al. (2022) and Jena et al. (2020) researched nanofluids, which demonstrated that non-uniform heat sources together with stretching surfaces and magnetic fields improve thermal transport properties. Fatunmbi and Salawu (2020) investigated entropy production during magneto-micropolar flow through porous materials with a nonuniform heat source, while Fatunmbi et al. (2023) researched electromagnetic actuators' melting heat transfer, and remarked that spatial heat production has a powerful effect on temperature distribution results. Alao et al. (2025) demonstrated that non-uniform energy generation results in substantial changes to temperature distribution and heat transfer performance during nanofluid flow through expanding porous channels. Fatunmbi and Adeniyan (2020) showed that MHD micropolar nanofluid flow experiences improved thermal boundary layer development through convective heating over stretching sheets. The mechanisms that produce these effects can be used to achieve optimal thermal performance and reliable operation in solar energy systems, electronic cooling systems, and chemical reactors.

Thermal radiation, representing heat transfer via electromagnetic waves, becomes increasingly significant under large temperature differences. Nonlinear radiation models provide more accurate predictions in high-temperature environments, such as solar energy systems, astrophysical flows, advanced electronic cooling, and glass or polymer manufacturing. In light of this, Guedri et al. (2023) reported enhanced heat transfer in micropolar nanofluid flow over contracting plates with nonlinear radiation; Makinde et al. (2017) analyzed melting heat transfer effects over expanding surfaces; Fatunmbi and Adeniyan (2020) reported improved thermal fields in magneto-micropolar flows with nonlinear radiation and entropy generation; Tong et al. (2021) extended these analyses to Oldroyd-B nanofluids with slip effects, activation energy, convective heating, and Cattaneo–Christov heat flux. Kumar et al. (2022) investigated MHD Casson fluid flow over a stretching surface with chemical reaction and nonlinear radiation, and showed that nonlinear radiation significantly enhances the thermal field and alters the boundary-layer behaviour. Hussain et al. (2023) numerically studied two-dimensional MHD flow including Joule heating and nonlinear thermal radiation, demonstrating that both effects strongly increase fluid temperature and influence heat-transfer characteristics. These studies confirm the important role of nonlinear radiation in MHD heat-transfer systems and provide a basis for further investigation under more complex physical models.

Research on free convective nanofluid flow has advanced significantly, as discussed above; however, researchers have not yet studied the combined effects of non-uniform heat sources, convective heating, and nonlinear thermal radiation on MHD nanofluid flow passing through vertically extending disks. Existing studies typically examine stretching sheets, cones, and plates operating under uniform heating, whereas practical systems employ heating elements that vary spatially and produce convection over different surfaces. These gaps motivated the current study. Thus, the present work investigates free convective MHD nanofluid flow over a vertically extending disk subjected to convective heating, chemical reaction coupled with activation energy, a space-and temperature-dependent heat source, and nonlinear radiation. The model is solved numerically, and graphical results illustrate the influence of key parameters on the flow fields. This analysis is significant for energy systems, industrial cooling applications, and advanced thermal management systems.

2. Methodology

The problem formulation and modelling are carried out under this section. Various assumptions for the developed model are stated: the similarity transformation quantities for the conversion of the partial derivatives into ordinary ones, the description of physical quantities of engineering usefulness, and the description of the method of solution to the transformed equations.

2.1 Problem Formulation and Modelling

The following assumptions provide a framework to analyze the combined influence of non-uniform heat source, convective heating, magnetic forces, nonlinear thermal radiation, nanoparticle transport, and chemical reactions on the flow and heat-mass transfer over a 3-D radially stretching disk.

- The flow is steady, incompressible, and laminar.
- The disk stretches linearly in both (x) and (y) directions, with corresponding velocities $(u_w = \beta x)$ and $(v_w = \beta y)$, where β denotes the stretching rate. The porous medium is a Darcy-Forchheimer type included in the momentum equation.
- Free convection arises due to temperature differences between the disk surface and the ambient fluid, while a uniform transverse magnetic field (B_0) is applied along the (z) −axis; induced magnetic fields are not accounted for in this study due to low magnetic Reynolds number.
- The disk surface is subjected to convective heating, allowing heat exchange with the surrounding fluid. The 3D radially stretching disk model accounts for radial expansion from the centre of the disk with a velocity proportional to radial distance.
- A non-uniform volumetric heat source is incorporated to represent spatially varying internal energy generation or absorption within the fluid and is denoted as Q'''.
- The thermal boundary layer experiences large temperature differences, necessitating the use of nonlinear thermal radiation expressed as: $\frac{16\sigma^*}{3k^*\rho c_p}\frac{\partial}{\partial z}\left(T^3\frac{\partial T}{\partial z}\right)$.
- The nanofluid consists of suspended nanoparticles, and the Buongiorno model is employed to account for Brownian motion and thermophoresis in the nanoparticle transport.
- The thermophysical properties of the base fluid are assumed constant, except in the buoyancy term in the momentum equation.
- A first-order irreversible chemical reaction with Arrhenius activation energy is included in the concentration field.

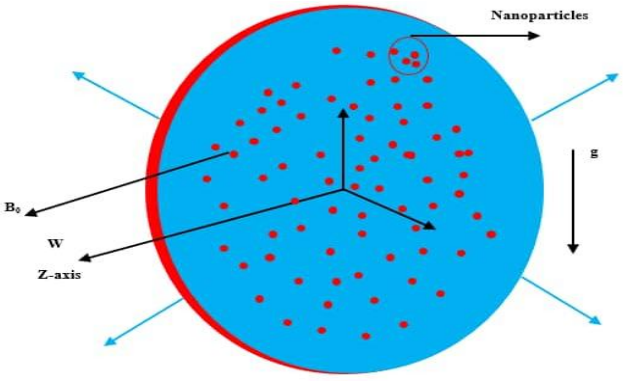

Figure 1: Diagrammatic representation of the flow configuration

2.2 Governing Equations

Incorporating the highlighted assumptions and using the well-known boundary layer, together with the Boussinesq approximations, the controlling equations are expressed in equations (1-6) (Ahmed et al., 2023; Wang, 2007, 2012).

$$\frac{\partial u}{\partial x}+\frac{\partial v}{\partial y}+\frac{\partial w}{\partial z}=0, \tag{1}$$

$$u\frac{\partial u}{\partial x}+v\frac{\partial u}{\partial y}+w\frac{\partial u}{\partial z}=\vartheta_f\left(\frac{\partial^2 u}{\partial x^2}+\frac{\partial^2 u}{\partial y^2}+\frac{\partial^2 u}{\partial z^2}\right)+g_1\,(T-T_\infty)$$
$$-\left(\frac{\sigma B_0^2}{\rho_f}\,u+\frac{\vartheta_f}{K_p}\,u+\frac{F_r}{K_p}u^2\right) \tag{2}$$

$$u\frac{\partial v}{\partial x}+v\frac{\partial v}{\partial y}+w\frac{\partial v}{\partial z}=\vartheta_f\left(\frac{\partial^2 v}{\partial x^2}+\frac{\partial^2 v}{\partial y^2}+\frac{\partial^2 v}{\partial z^2}\right)$$
$$-\left(\frac{\sigma B_0^2}{\rho_f}\,v+\frac{\vartheta_f}{Kp}\,v+\frac{F_r}{K_p}v^2\right) \tag{3}$$

$$u\,\frac{\partial w}{\partial x}+v\,\frac{\partial w}{\partial y}+w\,\frac{\partial w}{\partial z}=-\frac{1}{\rho}\frac{\partial p}{\partial z}+\vartheta_f\left(\frac{\partial^2 w}{\partial x^2}+\frac{\partial^2 w}{\partial y^2}+\frac{\partial^2 w}{\partial z^2}\right) \tag{4}$$

$$u\,\frac{\partial T}{\partial x}+v\,\frac{\partial T}{\partial y}+w\,\frac{\partial T}{\partial z}$$
$$=\frac{\kappa}{\rho_f c_p}\left(\frac{\partial^2 T}{\partial x^2}+\frac{\partial^2 T}{\partial y^2}+\frac{\partial^2 T}{\partial z^2}\right)+\frac{16\sigma^*}{3k^*\rho c_p}\frac{\partial}{\partial z}\left(T^3\frac{\partial T}{\partial z}\right)$$
$$+\frac{\mathrm{Q}'''}{\rho_f c_p}\tau_1\left[D_B\left(\frac{\partial C}{\partial x}\frac{\partial T}{\partial x}+\frac{\partial C}{\partial y}\frac{\partial T}{\partial y}+\frac{\partial C}{\partial z}\frac{\partial T}{\partial z}\right)\right.$$
$$\left.+\frac{D_t}{T_\infty}\left\{\left(\frac{\partial T}{\partial x}\right)^2+\left(\frac{\partial T}{\partial y}\right)^2+\left(\frac{\partial T}{\partial z}\right)^2\right\}\right] \tag{5}$$

$$u\frac{\partial C}{\partial x}+v\,\frac{\partial C}{\partial y}+w\,\frac{\partial C}{\partial z}$$
$$=D_B\left(\frac{\partial^2 C}{\partial x^2}+\frac{\partial^2 C}{\partial y^2}+\frac{\partial^2 C}{\partial z^2}\right)$$
$$+\frac{D_t}{T_\infty}\left\{\frac{\partial^2 T}{\partial x^2}+\frac{\partial^2 T}{\partial y^2}+\frac{\partial^2 T}{\partial z^2}\right\}$$
$$-\mathrm{cr}(C-C_\infty)\left(\frac{T}{T_\infty}\right)^n\exp\left(-\frac{E_a}{R_g T}\right) \tag{6}$$

The respective conditions at the wall for the controlling equations (1) - (6)

$$u(x,y,0)=u_w(x),v(x,y,0)=v_w(y),w(x,y,0)=0,$$
$$-\kappa\frac{\partial T}{\partial z}=\zeta^*(\mathrm{T_w}-T),C(x,y,0)=C_w,z=0; \tag{7}$$
$$u\to 0,v\to 0,T\to T_\infty,C\to C_\infty,P\to P_\infty,z\to\infty.$$

The term $Q'''=\frac{\kappa u_w}{x\vartheta_f}(T_w-T_\infty)[H_1 f'+\left(\frac{T-T_\infty}{T_w-T_\infty}\right)H_2]$ describes the nonuniform heat source/sink in the energy region. The components of spatial heat and thermal heat source are denoted as H_1 and H_2 respectively. More so, the respective components of velocities are $u_w(x)$ and $v_w(y)$ along the x and y directions. The conditions at the stretching surface $(z=0)$ assume that the fluid adheres to the surface and transports with those velocities in the x- and y-directions, and thus, the no-slip condition is assumed. The conditions at far field from the surface $(z\to\infty)$ signify that the stretching influence vanishes, and the fluid is quiescent in the free stream. More so, $Fr\ (=F_0x^{-1}),\beta_t$, and $\zeta^\star$ denote the Forchheimer porosity, coefficient of thermal expansion, and the temperature approaches the ambient value T_∞ while the nanoparticle concentration approaches the ambient value C_∞, indicating mass transfer equilibrium. The pressure approaches the free-stream pressure far from the surface $(P\to P_\infty)$.

2.3 Similarity variables for the transformation

Equation (8) consists of similarity transformation quantities, which are introduced into the controlling Equations (1–7) to transmute them into ordinary derivatives.

$$u=\left(\frac{\beta_t g_1(T_w-T_\infty)}{\beta}\right)g(\eta)+\beta x f'(\eta),$$

$$\begin{aligned} &v = \beta y f'(\eta), \frac{w}{2(\beta\vartheta_f)^{\frac{1}{2}}} = -f(\eta), \\ &(T - T_\infty)\theta(\eta) = \mathrm{T} - \mathrm{T}_\infty \\ &(C_w - C_\infty)\phi(\eta) = \mathrm{C} - C_\infty, \\ &\frac{\eta}{z} = \left(\frac{\beta}{\vartheta_f}\right)^{1/2} \end{aligned} \tag{8}$$

Upon substituting quantities (8) into equations (1-6) together with the wall conditions (7), the underlisted ODEs are obtained:

$$f'''(\eta) + 2\,f(\eta)\,f''(\eta) - (f'(\eta))^2 - (M+\delta)\,f'(\eta) - \mathrm{F_s f'^2(\eta)} = 0 \tag{9}$$

$$f'(\eta)G(\eta) - 2\,f(\eta)G'(\eta) - G''(\eta) + (M+\delta)\,G(\eta) - \mathrm{F_s G^2(\eta)} - \lambda\,\theta(\eta) = 0, \tag{10}$$

$$[1 + Nr(b-1)\theta + 1)^3]\theta''(\eta) + 3\big((b-1)\theta(\eta)\big)^2(b-1)\theta'^2 + 2Prf(\eta)\theta'(\eta) + [Q_1 f'(\eta) + Q_2\theta(\eta)] + \mathrm{Pr}[Nt(\theta')^2(\eta) + Nb\theta'(\eta)\phi'(\eta)] = 0 \tag{11}$$

$$\phi''(\eta) + 2Scf\phi'(\eta) + \frac{Nt}{Nb}\theta''(\eta) - Kr[(b-1)\theta(\eta)+1]^n \exp\left(\frac{E}{(b-1)\theta(\eta)+1}\right)\phi(\eta) = 0 \tag{12}$$

From the z-component of the momentum equation (4), the normalized pressure term is obtained thus:

$$p'(\eta) = -\rho\,\beta\,\vartheta_f\,(2\,f''(\eta) + 4\,f(\eta)f'(\eta)), \tag{13}$$

$$p(\eta) = -2\,\rho\,\beta\,\vartheta_f\,(f'(\eta) + f(\eta)^2) + C, \tag{14}$$

$$P(\eta) = \frac{p(\infty) - p(\eta)}{2\rho_f\beta\vartheta_f} = f(\eta)^2 + f'(\eta) - f(\infty)^2. \tag{15}$$

Moreover, equation (16) shows the transmuted wall conditions as:
At $\eta = 0$;

$$f(\eta) = 0, f'(\eta) = 1, G(\eta) = 0, \theta'(\eta) = -\zeta\big(1 - \theta(\eta)\big), \phi(\eta) = 1, \tag{16}$$

and

$$f(\infty) = 0, G(\infty) = 0, \theta(\infty) = 0, \phi(\infty) = 0.$$

Equation (18) is the emerging physical quantities derivable from the descriptive equations. Their descriptions are recorded in Table 1:

$$\begin{aligned} &M = \frac{\sigma B_0^2}{\beta\rho_f}, D_a = \frac{\vartheta_f}{\beta K_p}, \lambda = \frac{g_1\beta_t(Tw - T_\infty)}{\beta H}, Nr = \frac{16\sigma^* T_\infty^3}{k^\star\kappa}, \\ &Pr = \frac{(\mu_f c_p)}{\kappa}, b = \frac{T_w}{T_\infty}, Sc = \frac{\vartheta_f}{D_B}, Nt = \frac{\gamma D_t(T_w - T_\infty)}{\vartheta_f T_\infty}, \\ &Nb = \frac{\gamma D_B(C_w - C_\infty)}{\vartheta_f}, k_r = \frac{k_0}{\beta}, \gamma = \frac{E_a}{R_g T_\infty}, F_s = \frac{F_o}{K_p} \\ &Re_x = \frac{\beta x^2}{\vartheta_f}, H = \left(\frac{\beta_t g_0(T_w - T_\infty)}{\beta}\right)G(\eta), \zeta = \left(\frac{\sqrt{\zeta^{\star 2} z}}{\beta}\right) \end{aligned} \tag{17}$$

2.4 Quantities of Engineering Interest

The skin frictional factor, local Nusselt, and Sherwood numbers are included as the physical quantities of interest; they are respectively described as follows:

$$\begin{cases} C_{fx} = \dfrac{\tau_{wx}}{\rho(\beta x)^2} \\ Nu_x = \dfrac{xq_w}{\kappa(T_w - T_\infty)} \\ Sh_x = \dfrac{xj_w}{D_n(C_w - C_\infty)}. \end{cases} \tag{18}$$

The quantities τ_{wx}, q_w, and j_w are:

$$\begin{cases} \tau_{wx} = \mu_f\left(\dfrac{\partial u}{\partial z}\right)_{z=0} \\ q_w = -\kappa\left(\dfrac{\partial T}{\partial z}\right)_{z=0} \\ j_w = -D_B\left(\dfrac{\partial C}{\partial C}\right)_{z=0}. \end{cases} \tag{19}$$

The respective quantity in equation (19) is simply the wall shear stress, heat flux, and mass flux. Using the similarity transformation variables (9) to obtain the complete non-dimensional physical quantities expression:

$$\begin{cases} C_{fx}Re_x^{1/2} = f''(0) + \lambda G'(0) \\ Nu_x Re_x^{-1/2} = -\theta'(0) \\ Sh_x Re_x^{-1/2} = -\phi'(0). \end{cases} \tag{20}$$

The symbols and letters used for representing various quantities and parameters, as featured in Equations (1–21), are described in Table 1.

Table 1: Symbolic description of various letters and parameters.

Letters	Letters description	Letters	Letters description
u, v, w	Velocity components	T	Temperature
ϑ_f	Kinematic viscosity	n	Fitted rate constant
ρ_f	Fluid density	T_w	Surface temperature
μ_f	Fluid viscosity	Pr	Prandtl number
κ	Fluid thermal conductivity	b	Nonlinear thermal radiation parameter
σ	Electrical conductivity	T_∞	Free stream temperature
N_∞	Concentration at upstream	λ	Convective parameter
Nt	Thermophoresis parameter	Q_0	Coefficient of heat generation
k_r	Chemical rate of reaction	Sc	Schmidt number
C_w	Concentration at the upper disk	C	Concentration
Nb	Brownian term	E	Activation energy parameter
Kp	Permeability of the porous medium	δ	Porosity parameter
P	Pressure	Nr	Thermal radiation parameter
(ρc_p)	Heat capacity	g_1	Gravitational acceleration
κ	Thermal conductivity	F_s	Forchheimer term
E	Activation energy	Kr	Chemical reaction parameter
ζ	Biot number		

2.5 Solution Methodology

Due to the nonlinear nature of the controlling equations (9-12) with the wall conditions (16), a numerical solution is sought via the shooting technique together with the Runge-Kutta-Fehlberg method (RKFM).

This RKFM is a famous method which suitable for solving nonlinear differential equations. The shooting method is engaged to convert the BVP into an IVP by guessing the unknown initial conditions, integrating the system, and iteratively adjusting the guesses until the boundary conditions at infinity are satisfactorily obtained. The RKFM is then used to integrate the resultant set of first-order ordinary derivatives. The RKFM provides highly accurate, stable, and efficient results for nonlinear differential equations. It automatically adjusts the step size to maintain the desired error tolerance, making it particularly suitable for stiff or sensitive systems. Various authors have used RKFM and shooting methods in the literature due to their reliability and accurate numerical solutions. Unless otherwise stated, the computational parameter values employed in the current investigation are depicted as follows:

$$M = Nr = 0.5, Kr = 0.3, Pr = 7, \lambda = 0.5, Nt = 0.7, Sc = 0.62,$$
$$b = 1.5, = \mathrm{Q1} = \mathrm{Q2} = 0.2 = \zeta, \delta = 0.5 = Fs$$

We introduce the nine state variables:

$$\begin{cases} y_1(\eta) = f(\eta), y_2(\eta) = f'(\eta), y_3(\eta) = f''(\eta), \\ y_4(\eta) = G(\eta), y_5(\eta) := G'(\eta), \\ y_6(\eta) = \theta(\eta), y_7(\eta) := \theta'(\eta), \\ y_8(\eta) = \phi(\eta), y_9(\eta) = \phi'(\eta). \end{cases} \tag{22}$$

Using the definitions above, the equivalent first-order system $y_i' = F_i(\eta, y_1, \dots, y_9)$ is:

$$\begin{cases} y_1' = y_2, y_2' = y_3, \\ y_3' = -2\, y_1\, y_3 + y_2^2 + (M + \delta) y_2 + \mathrm{F_s} y_2^2, \\ y_4' = y_5, \\ y_5' = y_2\, y_4 - 2\, y_1\, y_5 + (M + \delta) y_4 + \mathrm{F_s} y_4^2 - \lambda y_6, \end{cases} \tag{23}$$

For the energy equation, we define the auxiliary coefficient:

$$B(y_6) := 1 + Nr((b-1)y_6 + 1)^3.$$

Then the equation for $y_7' = \theta''$ becomes:

$$y_7' = -\frac{1}{B(y_6)}(3((b-1)y_6 + 1)^2(b-1)\, y_7^2 + 2\mathrm{Pr}\, y_1\, y_7 + (\mathrm{Q}_1 y_2 + Q_2 y_6) + \mathrm{Pr}\, Nt\, y_7^2 + \mathrm{Pr}\, Nb\, y_7\, y_9) \tag{24}$$

Consequently, the concentration equation gives $y_9' = \phi''$. Upon substitution into the governing equation, we obtain:

$$\begin{aligned} y_8' &= y_9, \\ y_9' &= -2Sc\, y_1\, y_9 - \frac{Nt}{Nb} y_7' + kr((b-1)y_6 \\ &\quad + 1)^n \exp\left(\frac{\gamma}{(b-1)y_6 + 1}\right) y_8, \end{aligned} \tag{25}$$

For the boundary conditions, the transformed conditions both at the wall ($\eta = 0$) and at the far field $\eta \to \infty$ are:

At $\eta = 0$ (wall) and at the far field $\eta \to \infty$ are respectively given as:

$$\begin{cases} y_1(0) = 0, y_2(0) = 1, y_7(0) = -\zeta(1 - y_4(0)), y_6(0) = 1, y_8(0) = 1 \\ y_1(\infty) = 0, y_4(\infty) = 0, y_6(\infty) = 0, y_8(\infty) = 0 \end{cases} \tag{26}$$

Four initial derivatives are unspecified at $\eta = 0$, these are:

$$y_3(0) = f''(0) =: s_1, y_5(0) = G'(0) =: s_2, y_7(0) = \theta'(0) =: s_3,$$
$$y_9(0) = \phi'(0) =: s_4.$$

Thus, the IVP initial vector at $\eta = 0$ is:

$$\mathbf{Y}(0) = [\, 0, 1, s_1, 0, s_2, 1, s_3, 1, s_4\,]^{\mathrm{T}}.$$

Table 2 shows the computed values of the temperature gradient $-\theta'(0)$ and the tangential velocity gradient $G'(0)$ for different Prandtl numbers, as compared with previously published results (Ahmed et al., 2023; Wang, 2007). A good agreement is observed from the present findings as compared with previous data under some limiting scenarios.

Table 2: Computational values of $(-\theta'(0))$ and $G'(0)$ for variation of Pr as compared with published works when $R = M = Nt = E = Sc = \delta = n = 0, Nb = 0.0001, b = 1, Gr = 1$.

Pr	Wang (2007)		Ahmed *et al.* (2023)		Current work study	
	$-\theta'(0)$	$G'(0)$	$-\theta'(0)$	$G'(0)$	$-\theta'(0)$	$G'(0)$
0.2	0.25165	1.77962	0.254524	1.700592	0.250738	1.710367
0.7	0.66726	0.70658	0.666584	0.706789	0.667811	0.703440
2.0	1.32391	0.38407	1.323333	0.383630	1.323898	0.384067
7.0	2.72297	0.20331	2.726175	0.203049	2.722963	0.203307
20	4.78914	0.12164	4.840868	0.124378	4.789126	0.121645
70	9.18731	0.06593	8.430984	0.068906	9.187282	0.065928
200	15.7061	0.03933	15.966011	0.03701	15.706043	0.039329

3. Analysis of Results and their Discussion

To showcase the impact of various parameters, and for applications in relevant fields, various graphs are constructed in this section to demonstrate the trend of crucial parameters as they impacted the non-dimensional profiles of the physical field. The radial velocity profile diminishes with increasing M as pictured in Figure 3. This revelation points to the fact that the Lorentz force counteracts the buoyancy-driven upward motion, thereby reducing the intensity of natural convection. Consequently, an increase in M produces a thinner boundary layer and suppresses. Figure 3 illustrates the tangential velocity profile as M amplifies. suggesting that magnetic effects can be utilized to control thermal retention in magneto-nanofluid flow applications.

The picture reveals that an applied magnetic field suppresses the swirl motion of the electrically conducting fluid. As $G(\eta)$ tends to zero,

the profile is consistent with the far-stream wall condition, indicating that stronger magnetic fields effectively reduce the strength of rotational motion in the flow. Figure 4 is an exhibition of the heat profile as the strength of M rises in the system. There is a boost in the heat profile as revealed here. Such an occurrence stemmed from the frictional heating created by the Lorentz force, which acts as a resistive drag, reducing the fluid velocity and thereby decreasing convective heat transfer further from the disk, which thickens the thermal boundary layer. The electrically conducting nanofluid induces Ohmic heating, which correspondingly boosts the energy in the fluid. Consequently, an increase in M elevates the fluid temperature. The same trend, which is manifested in Figure 4, is shown in Figure 5. There is a thickened solutal bounding layer due to growth in M. Figures 6-9 showcase the trend of $Q1$ and $Q2$ on the thermal and tangential velocity profiles. Magnification of the space and thermal-dependent heat source, denoted as Q1 and Q2, respectively, causes both the heat profile and tangential velocity profiles to expand as noted in these pictures. In this case, a rise in these parameters causes additional heat in the system, thereby encouraging a rapid increase in the temperature distribution.

A rise in the porous parameter δ has an inverse effect on the radial velocity (Figure 10), whereas the tangential velocity field rises, corresponding to escalating growth in δ as noted in Figure 11. The reduction is due to the resistive Darcy drag of the porous medium, which opposes fluid motion and thickens the momentum boundary layer. Figure 12, on the other hand, manifests a growth in the temperature profile emanating from escalating values of δ. This decline lowers convective heat removal from the disk, while viscous and Ohmic dissipation within the porous medium adds energy to the fluid. In this case, higher values of this term enhance thermal retention in the magneto-nanofluid flow. Meanwhile, Figure 13 demonstrates a decline in the velocity field as the Forchheimer term (Fs) magnifies. This shows that there is further resistance to the fluid motion as Fs increases. Similarly, the axial velocity profile exhibits a downward trend as Fs amplifies, as depicted in Figure 14. However, there is a significant rise in the tangential velocity field as Fs grows in magnitude, as showcased in Figure 15. The picture of the impact of a mixed convection term λ on the tangential velocity is shown in Figure 16. There is a corresponding increase in the buoyancy force and a suppression of the viscous force as λ escalates in strength. Thus, a rise in this term accelerates the nanofluid motion. Figures 17, 18, and 19 show the impacts of Nt on the heat, tangential velocity, and concentration profiles. Observation reveals that there is a lift in all three profiles as Nt upsurges. In the physical sense, the term thermophoresis induces a migration of the nanoparticles from high-temperature regions to lower-temperature regions. This phenomenon improves the fluid momentum due to the extra particle flux, which slightly accelerates the tangential velocity.

Also, this migration causes an accumulation of nanoparticles near the surface and thereby raises the thermal energy within the boundary layer, which thus strengthens the heat distribution as depicted in Figure 17. Likewise, the nanoparticle concentration near the disk is enhanced due to the thermophoretic motion, thickening the concentration boundary layer. It is therefore confirmed that a higher intensity of Nt favours fluid transport mechanism as well as heat-mass transfer in the MHD nanofluid flow over a disk.

The thermal profile escalated due to the magnification of Kr (chemical reaction term) as displayed in Figure 20, whereas Figure 21 exhibits an opposite trend as Kr increases. This fact occurs because when Kr increases, it promotes the rate of the chemical reaction, which boosts the rate at which nanoparticles are consumed near the surface of the disk, hence reducing the concentration profile.

Figure 22 exhibits growth in the thermal region as the temperature ratio term (b) magnifies. This parameter denotes the ratio of the wall temperature to that of the ambient, and it is capable of capturing the large thermal difference in the flow field. In Figure 23, amplification of the activation energy term (E) indicates that the field of concentration significantly. This is because, with high activation energy, a significant amount of energy is required for a reaction to take place, thus a reduced rate, and hence the consumption of the species is reduced. This leads to an increase in the nanoparticle concentration profile $\phi(\eta)$.

However, a downward effect is shown on the concentration profile with a rise in this parameter, as noted in Figure 24. This behaviour occurs because a higher Nb intensifies the random motion of nanoparticles, thereby increasing microscopic energy exchange and promoting thermal energy transport in the fluid, and thus, the heat bounding surface layer increases. On the other hand, the concentration profile decreases with increasing this parameter because of the intensified random motion of nanoparticles, which promotes their diffusion away from the disk surface, thereby weakening nanoparticle accumulation near the wall and reducing concentration levels within the boundary layer.

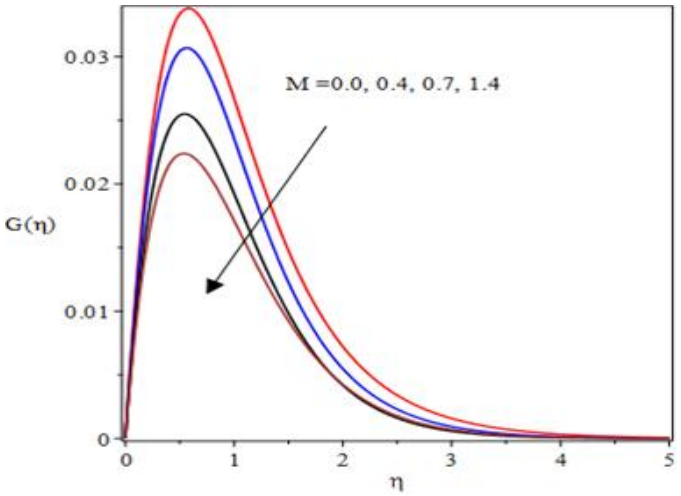

Figure 2: Trend of radial velocity for varying M.

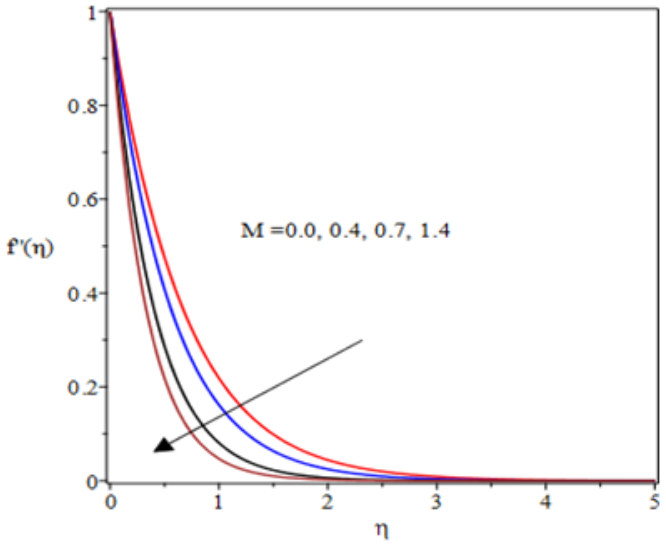

Figure 3: Plot of tangential velocity for M.

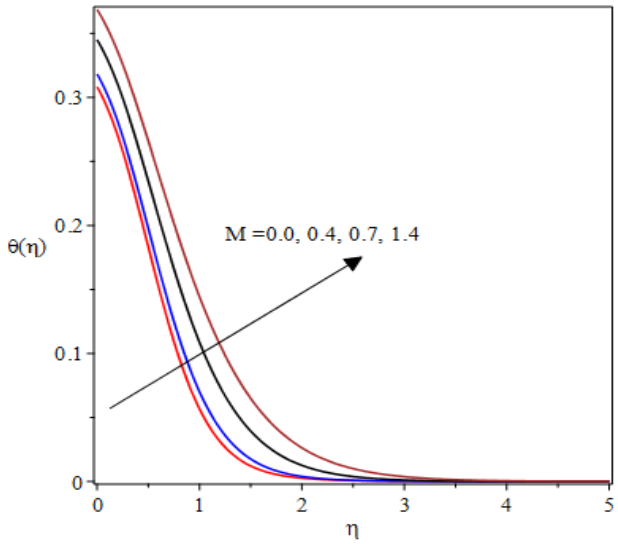

Figure 4: Heat profile for varying M.

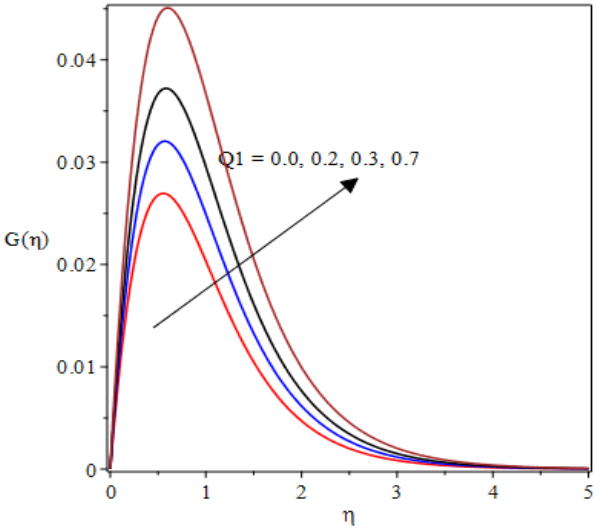

Figure 7: Tangential velocity for variation in $Q1$.

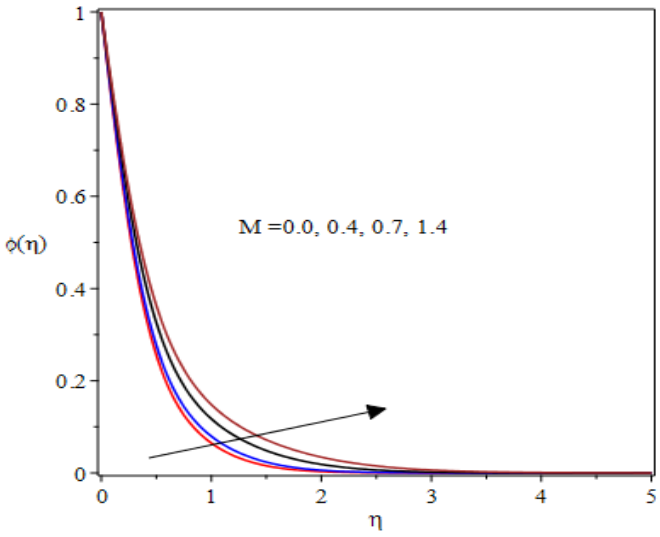

Figure 5: Concentration profile for variation in M.

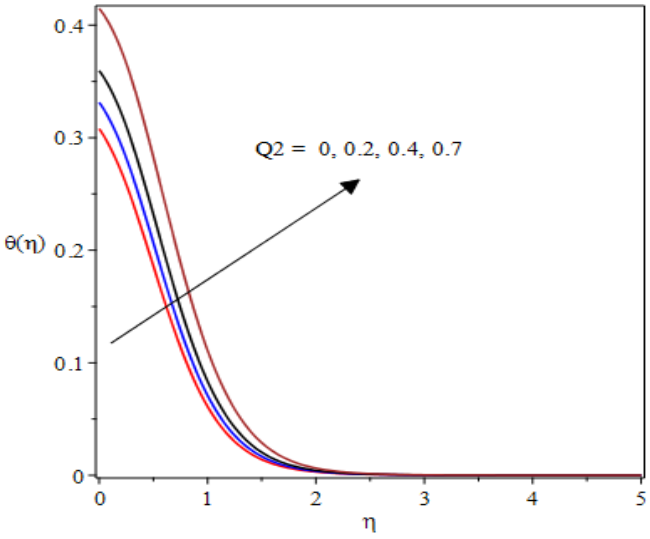

Figure 8: Heat profile for varying $Q2$.

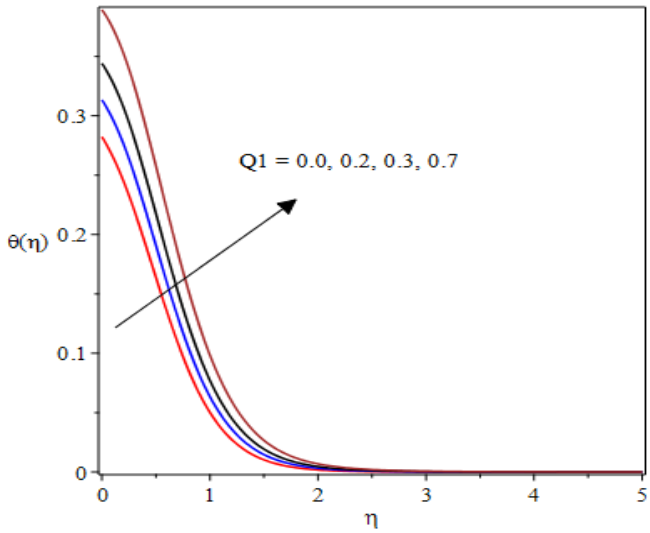

Figure 6: Heat profile for variation in $Q1$.

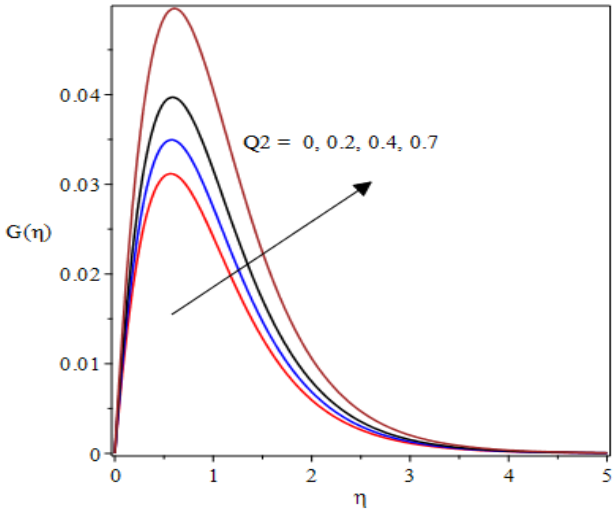

Figure 9: Tangential velocity profile for $Q2$.

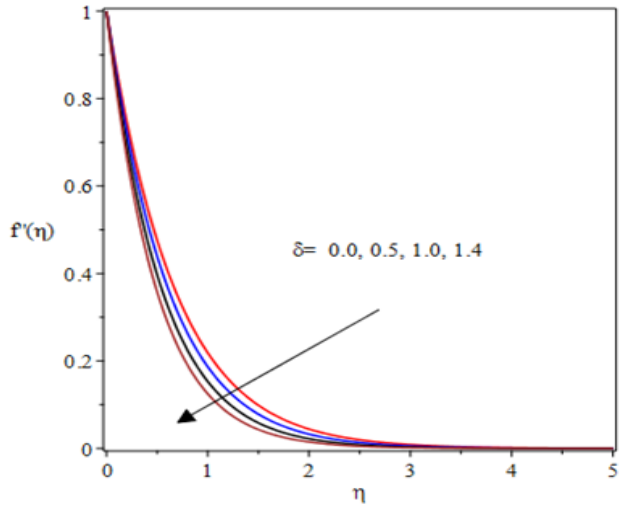

Figure 10: Radial velocity curve for δ.

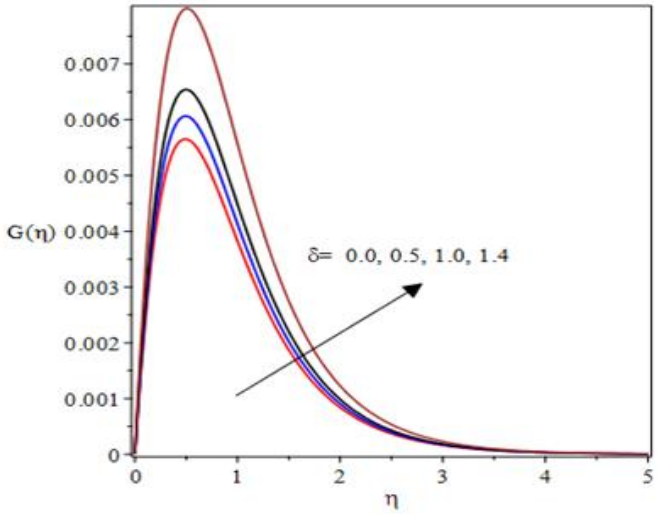

Figure 11: Tangential velocity curve for rising δ.

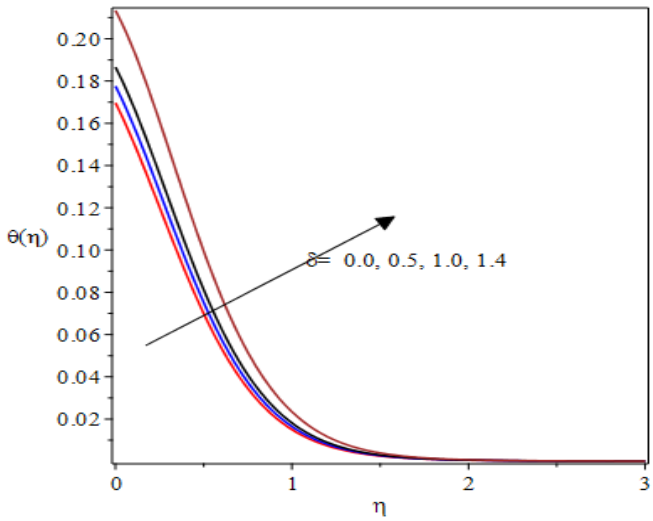

Figure 12: Radial velocity curve for δ.

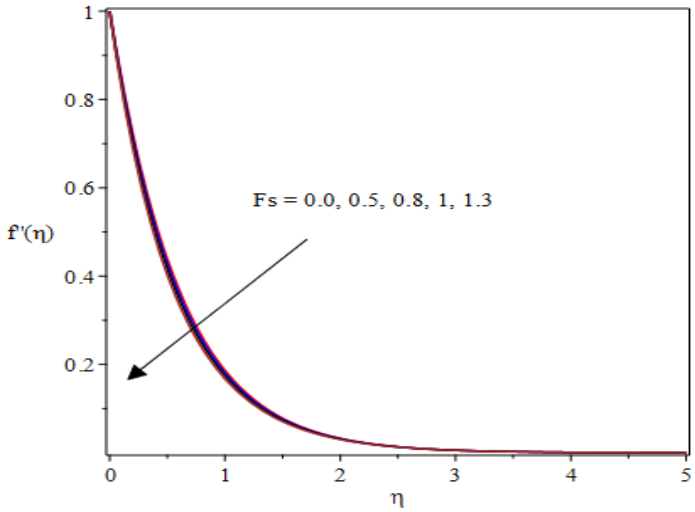

Figure 13: Radial velocity curve for rising Fs.

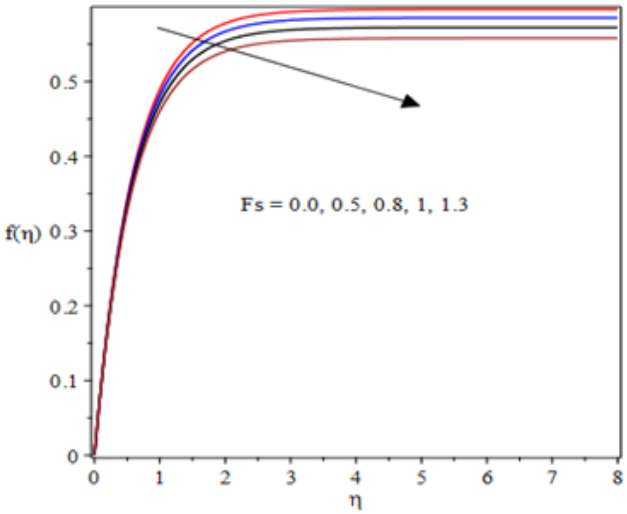

Figure 14: Axial velocity for varying Fs.

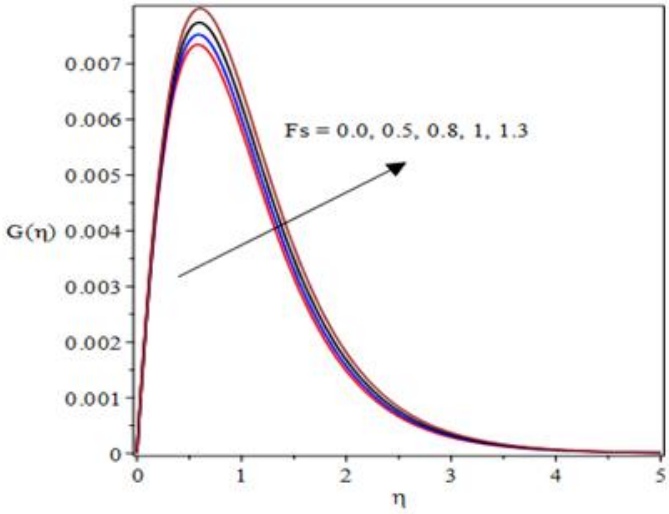

Figure 15: Tangential velocity profiles for Fs.

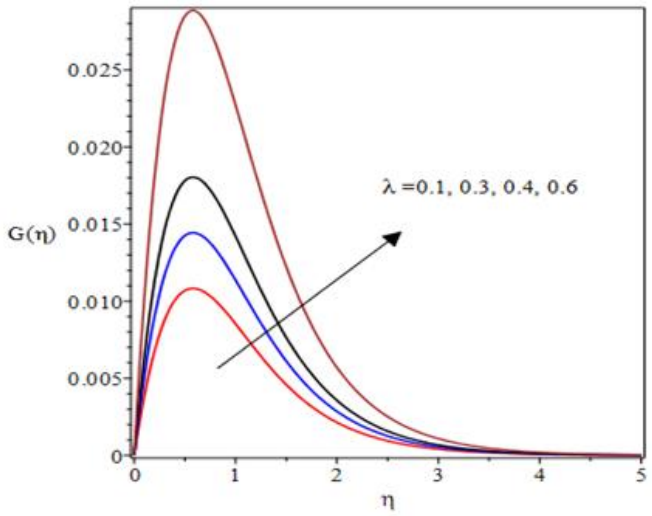

Figure 16: Tangential velocity for varying Nt.

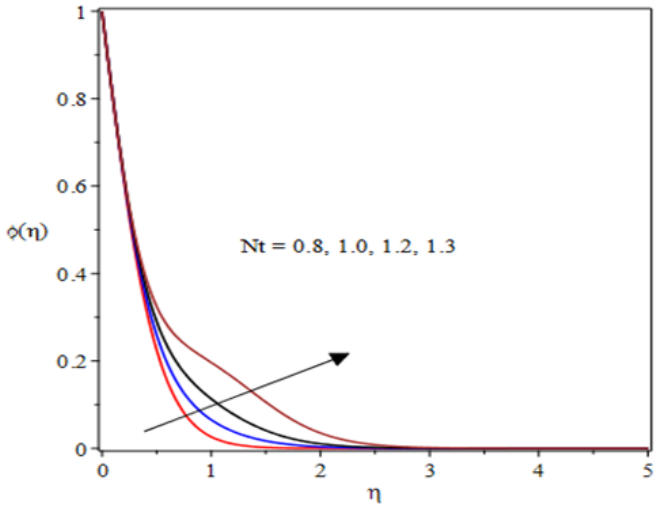

Figure 19: Concentration profiles for Nt.

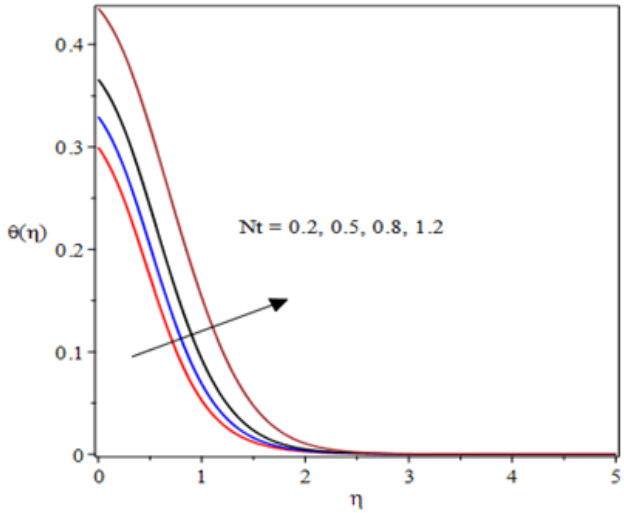

Figure 17: Thermal profiles for Nt.

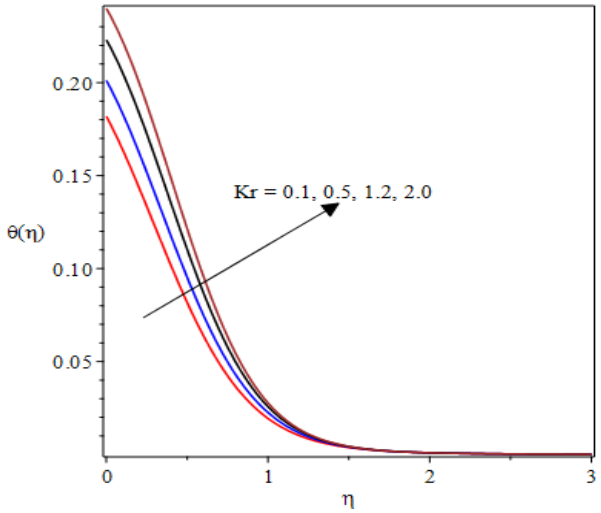

Figure 20: Thermal curve for varying Kr.

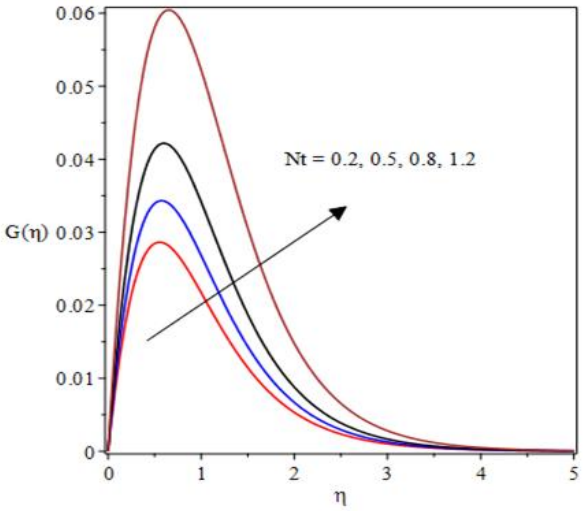

Figure 18: Tangential velocity for varying Nt.

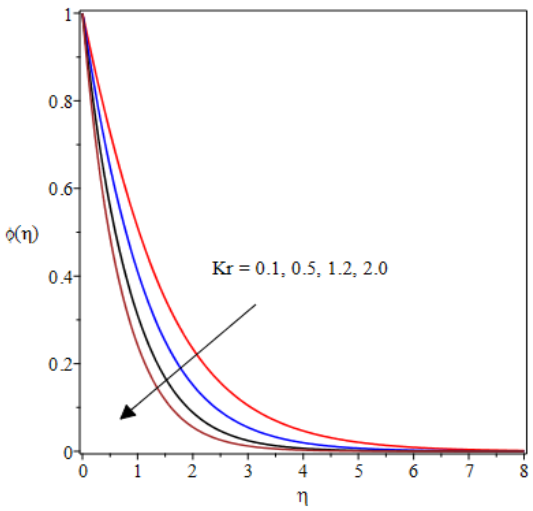

Figure 21: Concentration profiles for Kr.

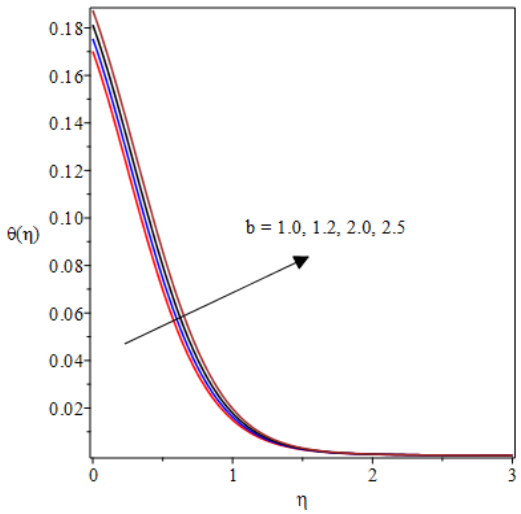

Figure 22: Thermal curve for varying b.

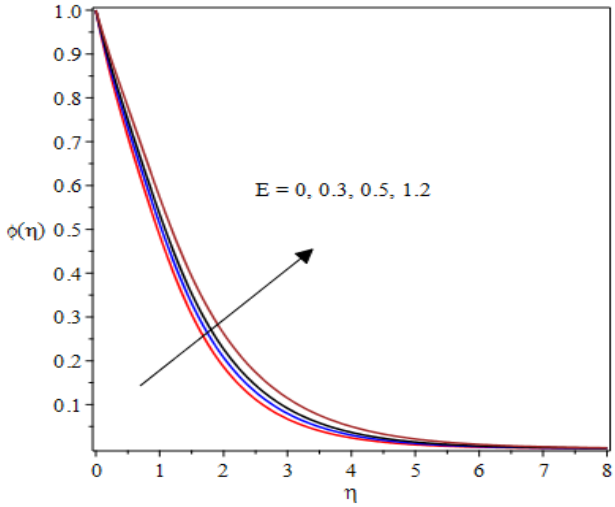

Figure 23: Concentration profiles for E

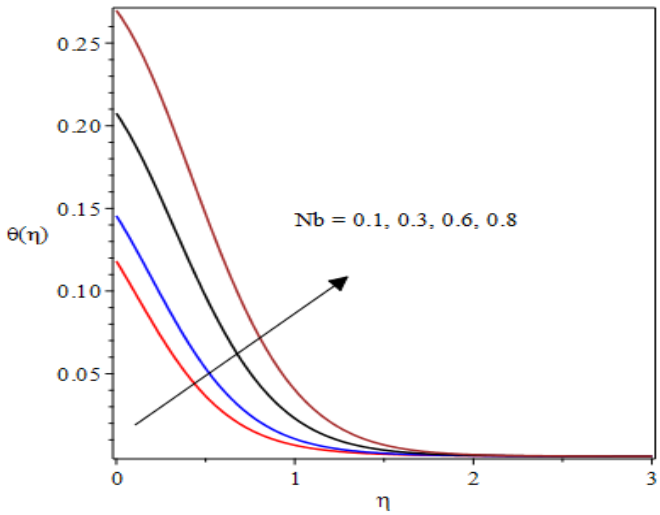

Fig. 24: Thermal curve for varying Nb

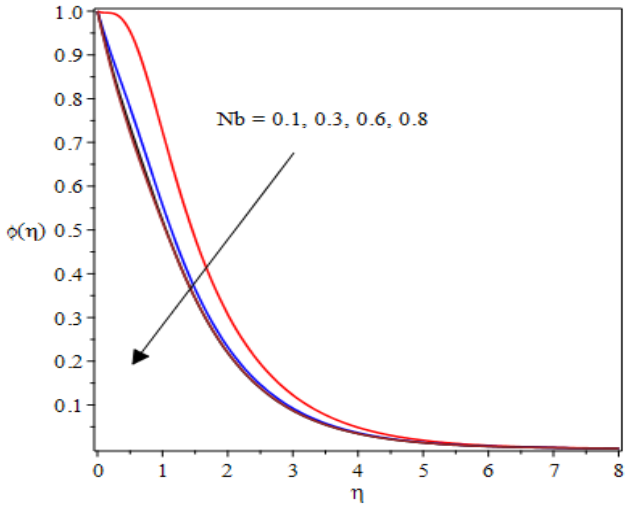

Figure 25: Concentration profiles for Nb.

The transport phenomenon of flow and heat-mass transfer properties of MHD free convection of nanofluid passing an expanding 3-D vertical disk is numerically addressed in this work. Conservation laws are employed to build the required model that fully describes the present problem. The equations are converted from their initial partial derivative forms into ordinary derivatives using suitable and appropriate similarity transformations. A stable and accurate numerical simulation is carried out via the shooting technique and the Runge–Kutta–Fehlberg integration scheme embedded in symbolic Maple software. The computational results are confirmed to be accurate by validating with previously published results under limiting conditions. Some of the crucial findings from this investigation are highlighted below:

- The inclusion of the thermophoresis parameter boosts both the thermal and nanoparticle concentration by driving particles toward cooler regions, thickening thermal and concentration boundary layers, whereas the concentration profile exhibited a declining nature owing to the Brownian motion term.
- There is a suppression of the velocity field profile by escalating values of the magnetic, porosity, and Forchheimer parameters, but the heat profile exhibited an opposite behaviour to this trend in that the temperature profile amplifies with these terms.
- Both spatial and thermal-dependent heat source significantly thickens the thermal bounding layer, affecting the temperature and heat transfer distribution in the system.
- The concentration boundary layer expands due to the rising values of the activation energy term, whereas the chemical reaction term diminishes the solutal profile and shrinks the solutal boundary layer.
- The tangential hydrodynamic boundary layer thickens as the Grashof number increases due to the strengthening of buoyancy forces, whereas the skin frictional factor declines as the porosity term amplifies.

The thermal boundary layer magnifies due to the growth in the nonlinear thermal radiation term and Brownian motion parameters, and thus the surface temperature rises.

Acknowledgments

The author appreciates the constructive comments of the anonymous reviewers, which helped improve the quality of this manuscript.

Funding

The author received no external funding and personally supported this research.

Competing Interest

The author affirms that there are no identifiable conflicts of interest, either financial or personal, that could be perceived as influencing the work presented in this paper.

Data Availability Statement

All data generated or analyzed during this study are included in this published article.

Ethics Approval

This study is theoretical and numerical, therefore, ethics approval was not required.

References

Abro, K. A. (2020). Fractional characterization of fluid and synergistic effects of free convective flow in circular pipe through Hankel transform. Physics of Fluids, 32(12). https://doi.org/10.1063/5.0034012

Abro, K. A., Siyal, A., Souayeh, B., & Atangana, A. (2020). Application of statistical method on thermal resistance and conductance during magnetization of fractionalized free convection flow. International Communications in Heat and Mass Transfer, 119, 104971.

Ahmed, A., Usman, M., Lu, D., Zhang, Z., Hussien, M. A., & Hassan, A. M. (2023). Numerical simulation of free convective flow over vertical disk via spectral-collocation method. Case Studies in Thermal Engineering, 52, 103668 https://doi.org/10.1016/j.csite.2023.103668

Alao, S., Ogunmola, O. J., Oderinu, R. A., Sulaiman, N. G., & Oyewumi, A. A. (2026). Numerical investigation of magnetohydrodynamics (MHD) mixed convective nanofluid (Ag and Fe2O3) flow through a stretchy/shrinky microchannel with non-uniform heat generation or absorption using the Tiwari-Das model. International Journal of Ambient Energy, 47(1), 2628878.

Alao, S., Salawu, S. O., Oderinu, R. A., Akinola, E. I., Oyewumi, A. A., Yahaya, A. A., & Salaudeen, K. A. (2025). Numerical computation of thermal radiation and mixed convective effect on electro-magnetized Tiwari–Das nanofluid model in a porous microchannel. International Journal of Applied and Computational Mathematics, 11(3), 113. https://doi.org/10.1007/s40819-025-01314-8

Anantha Kumar, K., Venkata Ramudu, A. C., Sugunamma, V., & Sandeep, N. (2022). Effect of non-linear thermal radiation on MHD Casson fluid flow past a stretching surface with chemical reaction. International Journal of Ambient Energy, 43(1), 8400-8407.

Dogonchi, A. S., Chamkha, A. J., Seyyedi, S. M., Hashemi-Tilehnoee, M., & Ganji, D. D. (2019). Viscous dissipation impact on free convection flow of Cu-water nanofluid in a circular enclosure with porosity considering internal heat source. Journal of Applied and Computational Mechanics, 5(4), 717-726.

Choi, S. U. (1995). Enhancing thermal conductivity of fluids with nanoparticles. In ASME International Mechanical Engineering Congress and Exposition (Vol. 17421, pp. 99–105). American Society of Mechanical Engineers.

Devendiran, D. K., & Amirtham, V. A. (2016). A review on preparation, characterization, properties and applications of nanofluids. Renewable and Sustainable Energy Reviews, 60, 21–40. https://doi.org/10.1016/j.rser.2016.01.115

Dinarvand, S., & Pop, I. (2017). Free-convective flow of copper/water nanofluid about a rotating down-pointing cone using Tiwari–Das nanofluid scheme. Advanced Powder Technology, 28(3), 900–909. https://doi.org/10.1016/j.apt.2017.01.007

Fatunmbi, E. O., & Adeniyan, A. (2020). Nonlinear thermal radiation and entropy generation on steady flow of magneto-micropolar fluid passing a stretchable sheet with variable properties. Results in Engineering, 6, 100142. https://doi.org/10.1016/j.rineng.2020.100142

Fatunmbi, E. O., & Salawu, S. O. (2020). Thermodynamic second law analysis of magneto-micropolar fluid flow past nonlinear porous media with non-uniform heat source. Propulsion and Power Research, 9(3), 281-288.

Fatunmbi, E. O., Adeosun, A. T., & Salawu, S. O. (2023). Dynamics of melting heat transfer of a micropolar nanofluid over an electromagnetic actuator with irregular thickness and non-uniform heat source. International Journal of Applied and Computational Mathematics, 9(3), 45.

Fatunmbi, E. O., Mabood, F., Elmonser, H., & Tlili, I. (2020). Magnetohydrodynamic nonlinear mixed convection flow of reactive tangent hyperbolic nanofluid passing a nonlinear stretchable surface. Physica Scripta, 96(1), 015204.

Fatunmbi, E. O., Oke, A. S., & Salawu, S. O. (2023). Magnetohydrodynamic micropolar nanofluid flow over a vertically elongating sheet containing gyrotactic microorganisms with temperature-dependent viscosity. Results in Materials, 19, 100453. https://doi.org/10.1016/j.rinmat.2023.100453

Fatunmbi, E. O., Salawu, S. O., & Adeniyan, A. (2022). Buoyancy force and slip conditions on hydromagnetic dissipative flow of micropolar fluid passing an exponentially stretching sheet. Computational Thermal Sciences,14(1), 1-13.

Fatunmbi, E. O., Salawu, S. O., & Adeniyan, A. (2022). Buoyancy force and slip conditions on hydromagnetic dissipative flow of micropolar fluid passing an exponentially stretching sheet. Computational Thermal Sciences: An International Journal, 14(1).

Guedri, K., Mahmood, Z., Fadhl, B. M., Makhdoum, B. M., Eldin, S. M., & Khan, U. (2023). Mathematical analysis of nonlinear thermal radiation and nanoparticle aggregation on unsteady MHD flow of micropolar nanofluid over shrinking sheet. Heliyon, 9(3), e13344. https://doi.org/10.1016/j.heliyon.2023.e13344

Hussain, F., Nazeer, M., Mengal, A., Hussain, A., & Shah, S. A. R. (2023). Numerical simulation of MHD two-dimensional flow incorporated with Joule heating and nonlinear thermal radiation. ZAMM-Journal of Applied Mathematics and Mechanics/Zeitschrift für Angewandte Mathematik und Mechanik, 103(6), e202100246.

Jena, S., Mishra, S. R., & Pattnaik, P. K. (2020). Development in the heat transfer properties of nanofluid due to the interaction of inclined magnetic field and non-uniform heat source. Journal of Nanofluids, 9(3), 143-151.

Jha, B. K., Altine, M. M., & Hussaini, A. M. (2022). Role of suction/injection on free convective flow in a vertical channel in the presence of point/line heat source/sink. Journal of Heat Transfer, 144(6), 062602. https://doi.org/10.1115/1.4053984

Kumar, D., Singh, A. K., and Kumar, D. Eect of hall current on the magnetohydrodynamic free convective ow between vertical walls with induced magnetic eld. The European Physical Journal Plus, 133(5):207, 2018. https://doi.org/10.1140/epjp/i2018-12146-5

Mishra, A., & Kumar, M. (2021). Numerical analysis of MHD nanofluid flow over a wedge including viscous dissipation and heat generation/absorption using the Buongiorno model. Heat Transfer, 50(8), 8453–8474. https://doi.org/10.1002/htj.22079

Mustafa, M., Khan, J. A., Hayat, T., & Alsaedi, A. (2017). Buoyancy effects on the MHD nanofluid flow past a vertical surface with chemical reaction and activation energy. International Journal of Heat and Mass Transfer, 108, 1340–1346. https://doi.org/10.1016/j.ijheatmasstransfer.2016.11.018

Muthtamilselvan, M., Periyadurai, K., & Doh, D. H. (2017). Effect of uniform and nonuniform heat source on natural convection flow of micropolar fluid. International Journal of Heat and Mass Transfer, 115, 19-34.

Nadeem, S., Khan, A. U., & Saleem, S. (2016). A comparative analysis of different nanofluid models for oscillatory stagnation point flow. The European Physical Journal Plus, 131(8), 261. https://doi.org/10.1140/epjp/i2016-16261-4

Seth, G. S., Bhattacharyya, A., & Mishra, M. K. (2019). Study of partial slip mechanism on free convection flow of viscoelastic fluid past a nonlinearly stretching surface. Computational Thermal Sciences: An International Journal, 11(1-2).

Tong, Z. W., Khan, S. U., Vaidya, H., Rajashekhar, R., Sun, T. C., Khan, M. I., Prasad, K. V., Chinram, R., & Aly, A. A. (2021). Nonlinear thermal radiation and activation energy significances in slip flow of bioconvection of Oldroyd-B nanofluid with Cattaneo–Christov theories. Case Studies in Thermal Engineering, 26, 101069. https://doi.org/10.1016/j.csite.2021.101069

Turkyilmazoglu, M. (2017). Condensation of laminar film over curved vertical walls using single and two-phase nanofluid models. European Journal of Mechanics – B/Fluids, 65, 184–191. https://doi.org/10.1016/j.euromechflu.2017.06.001

Turkyilmazoglu, M. (2021). On the transparent effects of Buongiorno nanofluid model on heat and mass transfer. The European Physical Journal Plus, 136(4), 1–5. https://doi.org/10.1140/epjp/s13360-021-01215-1

Umavathi, J. C., Chamkha, A. J., & Mohiuddin, S. (2016). Combined effect of variable viscosity and thermal conductivity on free convection flow of a viscous fluid in a vertical channel. International Journal of Numerical Methods for Heat & Fluid Flow, 26(1), 18-39.

Wang, C. Y. (2007). Natural convection on a vertical radially stretching sheet. Journal of mathematical analysis and applications, 332(2), 877-883.

Wang, C. Y. (2012). Natural convection on a vertical stretching cylinder. Communications in Nonlinear Science and Numerical Simulation, 17(3), 1098-1103.

How to Cite: Fatunmbi, E.O. (2026). Magnetohydrodynamic Free Convection Nanofluid Flow over a Convectively Heated Vertical Disk with Non-Uniform Heat Generation and Nonlinear Radiation. *Science Research Annals–Physical Sciences,* 2(1), 1–12. https://doi.org/10.63112/ne611a08